Geophysical Research Letters

Supporting Information for

Rapid basal channel growth beneath Greenland's longest floating ice shelf

Ash Narkevic[1], Bea Csatho[1], Toni Schenk[1]

[1]Department of Geological Sciences, University at Buffalo, Buffalo, NY, USA

Contents of this file

Text S1 to S5
Figures S1 to S9
Tables S1 to S2

Introduction

This supplement contains supporting text, figures, and tables for "Rapid basal channel growth beneath Greenland's longest floating ice shelf."

Text S1. Ice sheet and ice shelf elevation from 1978-2020

The AERODEM tiles in the N79 region are derived from aerial photographs collected in July 1978. The AERODEM has a horizontal resolution of 25 m, a horizontal error of 10 m and a vertical error of 6 m, with vertical errors increasing from the coastal regions toward the interior (Korsgaard et l., 2016).

The WV DEMs have an original resolution of 2 m, and errors (both vertical and horizontal) are estimated to be around 4 m (Porter et al., 2022).

All DEMs are referenced to the WGS-84 ellipsoid and provided in UTM N-27 projection. Prior to correcting them we resampled the WV DEMs to 30 m resolution.

The uncertainty of a corrected WV DEM (δh_{DEM}) is derived derived from the respective uncertainties of the correction surface fitting (δh_c^2), and the time series curve fitting (δh_t^2), both of which as taken as the standard deviation of residuals according to:

$$\delta h_{DEM} = \sqrt{\delta h_c^2 - \delta h_t^2}$$

and is typically on the order of ~1m, which is a significant improvement over the original ~4m error.

Text S2 Corrections of floating ice elevations

The tide correction portion of the software used for these reconstructions is adapted from that used by Sutterly et al. (2019) using the tidal model of Padman et al. (2018). A tidal correction is applied to ice elevations at all points that are not grounded, however, it is assumed the effect is dampened near the grounding line and the sides of the outlet glacier. From InSAR measurement a tidal flexure zone extending 6 km downstream beyond the grounding line was detected in March 5, 2017 (ESA, 2017), and GPS measurements suggested a few km wide flexure zones inward from the fjord walls (Reeh et al., 2000). We used conservative estimates of 10 km and 2 km for the flexure zone width along the grounding line and the fjord walls, respectively. Within these zones, the tidal correction is scaled in a linear fashion from 100% of the modeled correction to 0% at the grounding line/fjord walls.

A correction is also applied to offset the inverse barometric effect:

$$\Delta IBE = \frac{p_{avg} - p_{loc}}{\rho_w g}$$

where p_{avg} is the global average atmospheric pressure, p_{loc} is the local atmospheric pressure, ρ_w is the density of seawater, and g is gravitational acceleration. Currently, this correction is only applied to ICESat and ICESat-2 data, as ATM data products do not include corresponding modeled atmospheric pressure information. For the example time series in Fig. S3 these corrections improved the standard deviation of the polynomial fit residual from 0.445 m to 0.216 m, and the standard deviation of the penalized spline fit residual (ALPS; Shekhar et al., 2021) from 0.336 m to 0.135 m.

Text S3. Ice Bottom Reconstruction

Additionally, the bathymetry used to infer grounding lines from the ice bottom reconstruction is taken from An et al. (2020). An assumption of hydrostatic equilibrium is made to reconstruct the elevation of the ice bottom from the ice surface DEMs. First, the DEMs are converted from the WGS-84 ellipsoid used by ArcticDEM strips and the ice sheet altimetry to the EIGEN-6C4 geoid (Foerste et al., 2014) to obtain the ice elevation above sea level. Densities of 1026 kg/m^3 for sea water and 917 kg/m^3 for glacier ice are assumed, thus making the estimated depth

8.4128 times greater than the surface elevation. If the calculated ice bottom elevation is below the bedrock elevation at a given location, the glacier is assumed to be grounded at that location, and the bed elevation is used as the ice bottom elevation.

Reconstructing the ice bottom in this manner creates a bottom surface that is extremely rugged, as the surface DEM captures many small-scale features which are likely to be out of precise equilibrium. Therefore, a gaussian filter with a kernel size of 21 pixels (equivalent to 600 meter) is applied to the ice bottom reconstructions presented in this paper.

The uncertainty of this data set is estimated by direct comparison with the radar measurements. The difference between the radar pick and calculated ice bottom after smoothing is calculated along a segment of the ice bottom that is relatively flat (18000 m – 25000 m in the 4/29/2014 radar profile in Fig. S4). The standard deviation of these differences is found to be 9.4m, and this is taken as representative of regions of the ice where the assumption of hydrostatic equilibrium is valid. Additionally, the mean difference was found to be 0.91m, suggesting minimal bias in this sample.

Text S4. Calculation of elevation change in a Lagrangian (moving) reference frame

In the final Lagrangian elevation change data product, the listed value is positioned at the end of the movement of the ice parcel. I.e., for a given starting pixel, the corresponding ending pixel is estimated using the velocity, and the difference between these two elevations is reported as the Lagrangian elevation change at the ending pixel (Fig. S6, floating ice).

The DEM reconstruction dates (Table S1) are generally representative of spring, and the annual velocity products used are the average from July 1st of one year to June 30th of the following year.

Text S5. Runoff Evolution

To quantify the change in runoff within the N79 drainage basin over time, it was first necessary to demarcate the extent of that basin. TopoToolbox lacked this functionality, so for these purposes the drainage reconstruction was performed in ArcMap. Since full DEMs exist only for a limited number of years, it is assumed that the subglacial drainage basin extent is static, and the 2017 DEM and bed DEM were used to calculate it. For each year from 1978 to 2016, all pixels within these bounds were identified in the RACMO v2.3p2 runoff dataset and summed. The results are illustrated in Fig. S8.

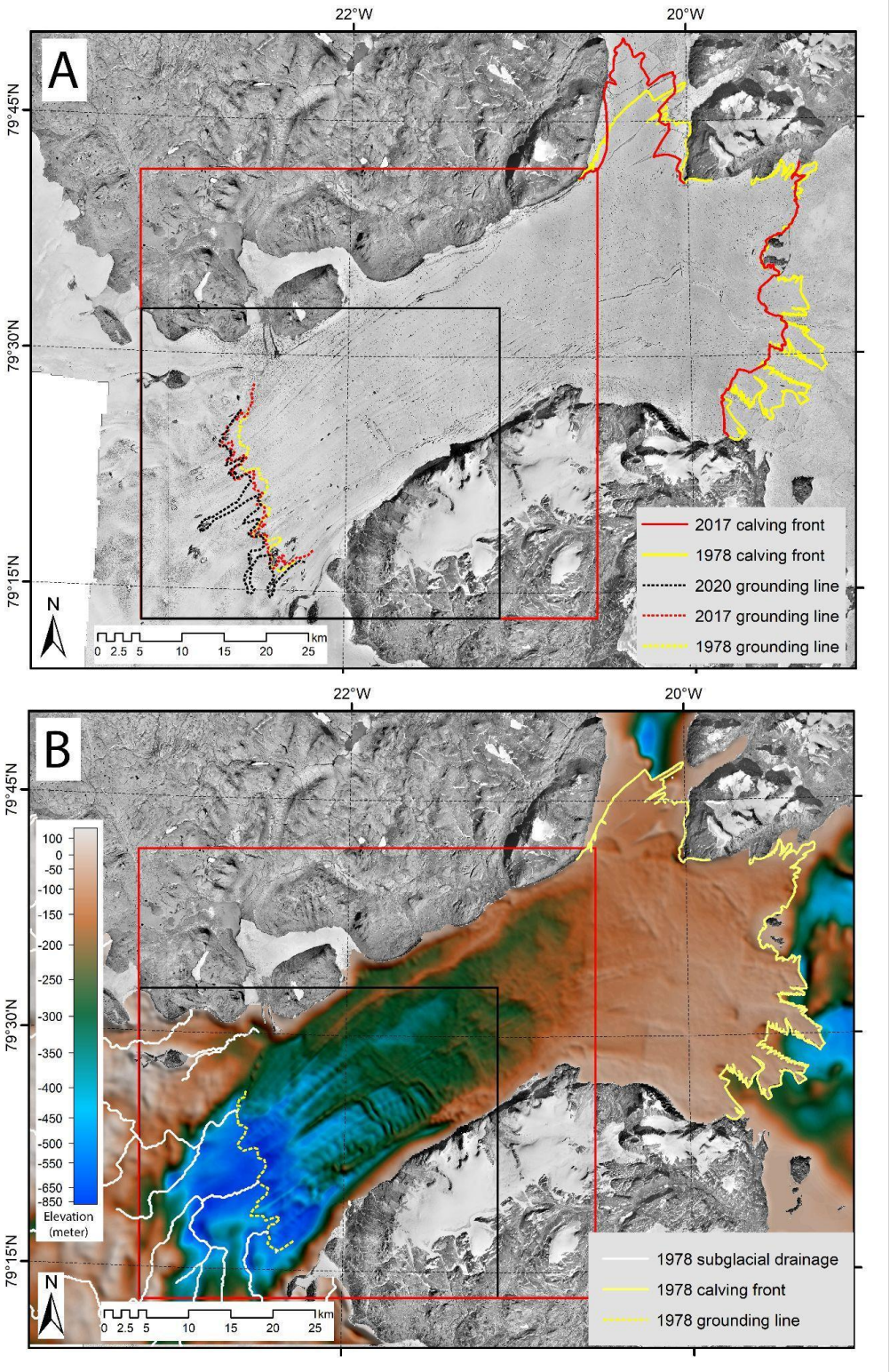

Figure S1. Surface features and ice bottom topography of N79 in 1978. (A) Aerial photo orthomosaic, (B) elevation of the ice bottom under the floating tongue, combined with bedrock elevation under the grounded ice sheet and the ocean.

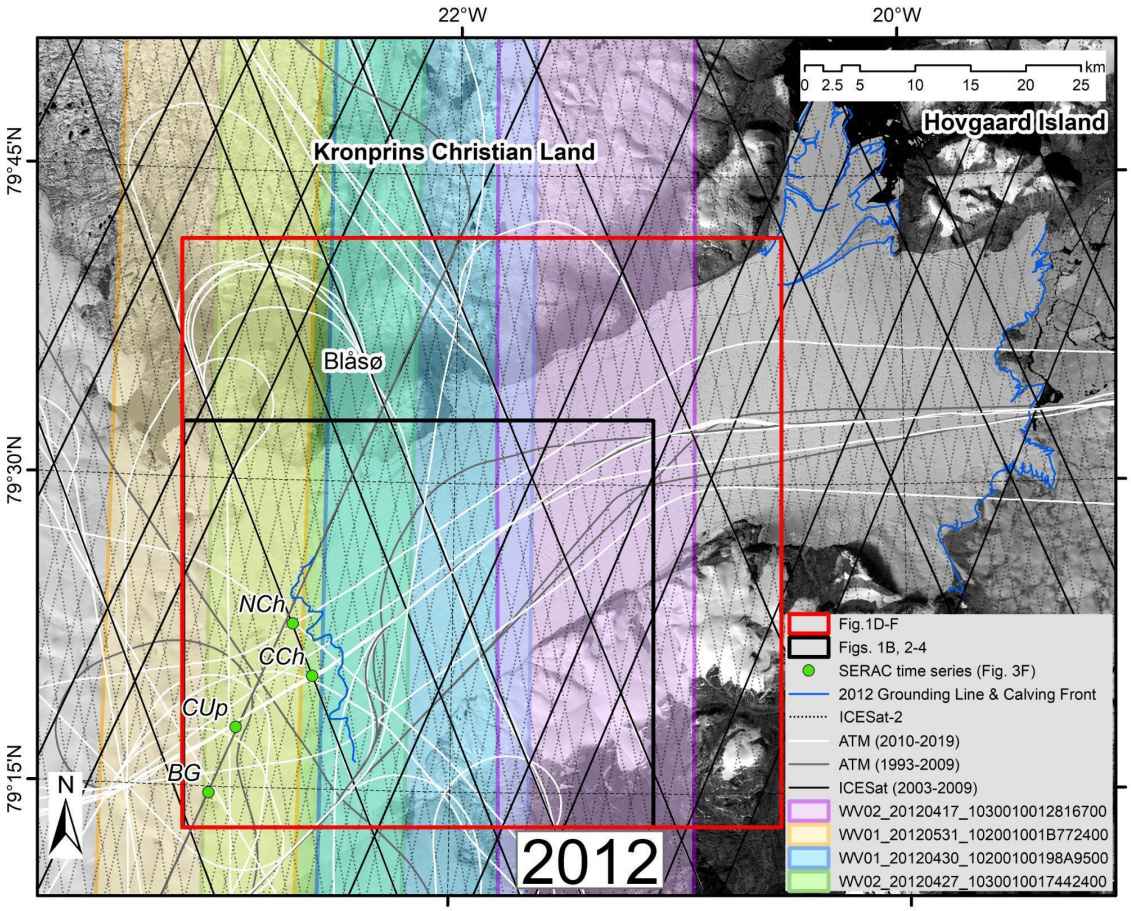

Figure S2. Location of four 2012 WorldView DEMs from a total of 14 used for generating the 2012 ice sheet elevation reconstruction (see Table S1 for complete list) with altimetry data locations (ATM, ICESat, ICESat-2) overlain. Background is a Landsat-8 imagery mosaic.

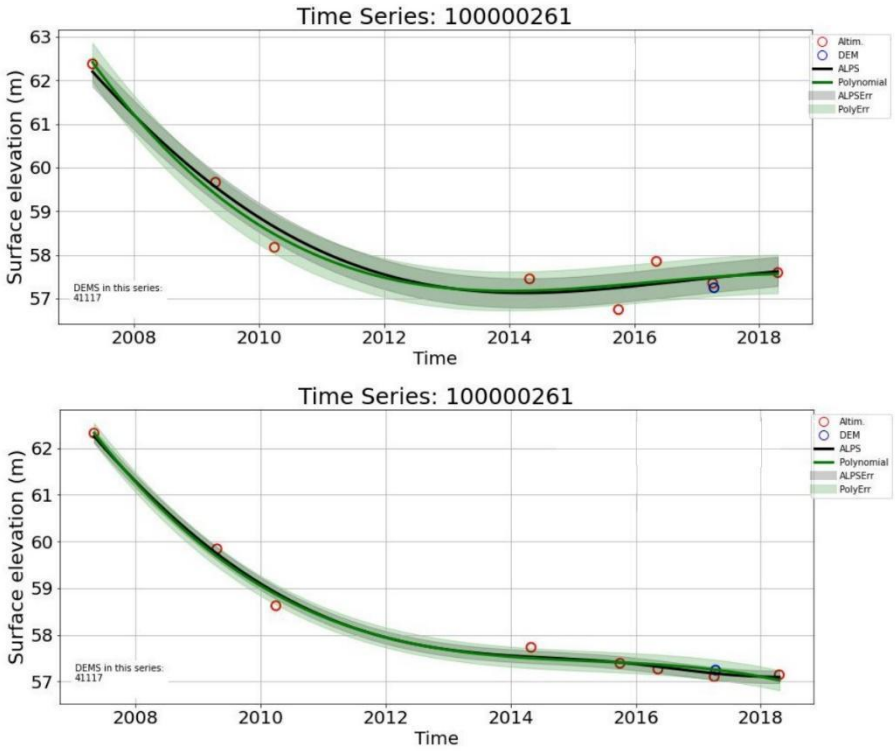

Figure S3. A typical altimetry time series on floating ice before (top) and after (bottom) tidal and barometric corrections are applied.

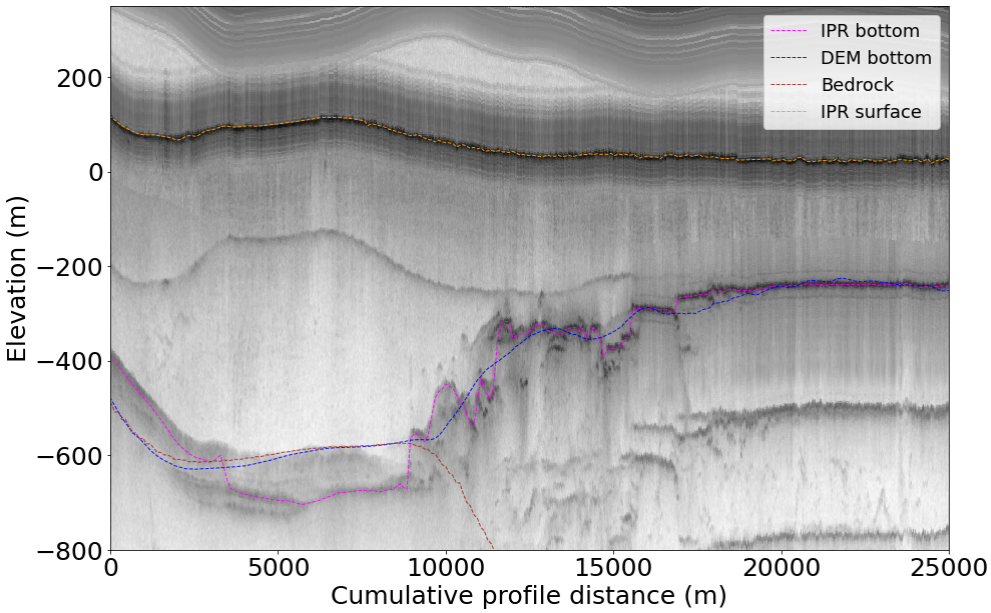

Figure S4. Radar profile from 4/29/2014 (IPR2-IPR2', Figure 3B) used to estimate the uncertainty of the calculated ice bottom depth.

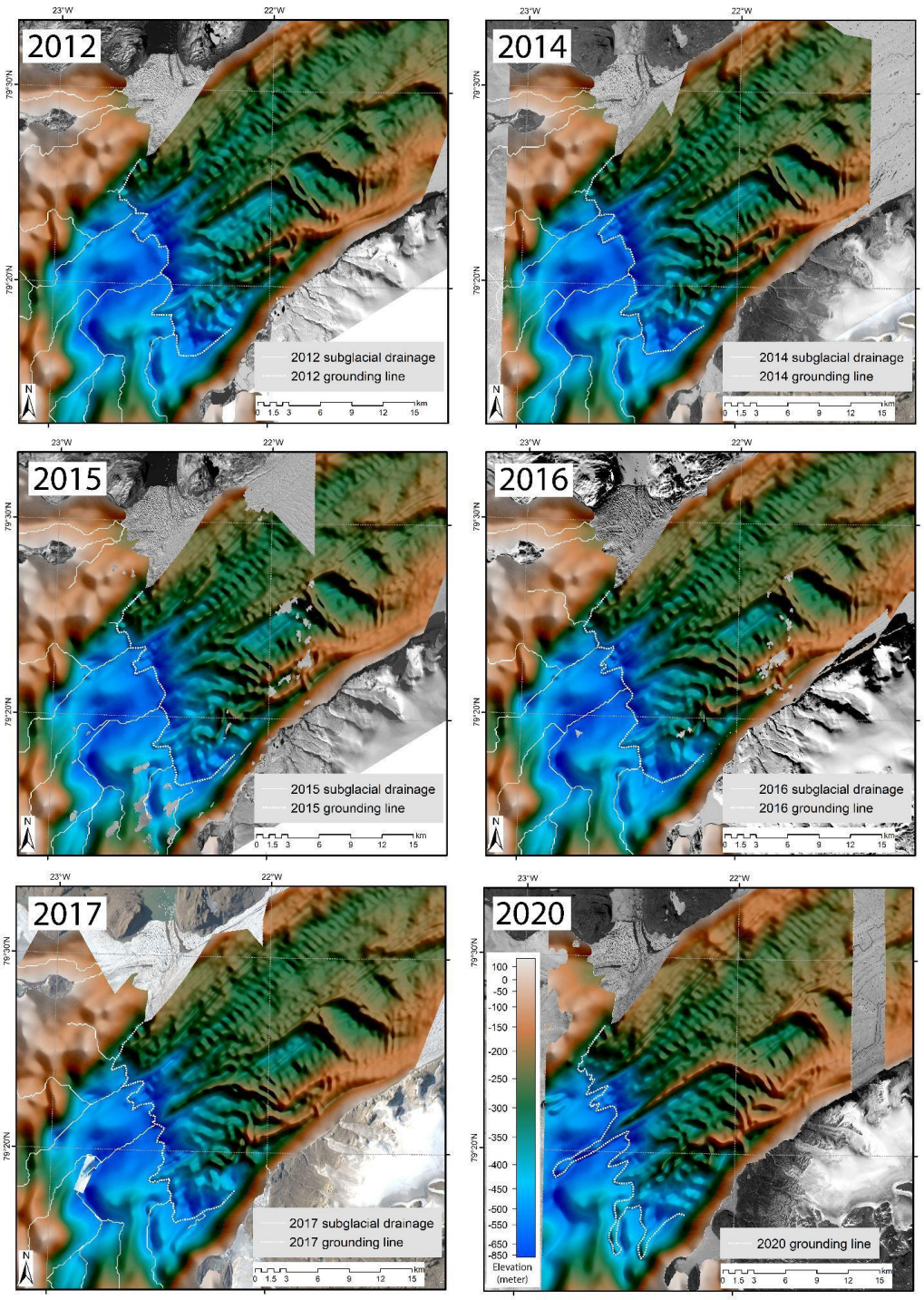

Figure S5. Ice sheet bottom at the grounding zone region in 2012, 2014, 2015, 2016, 2017 and 2020. Elevation of the ice bottom is shown under the floating tongue and bedrock elevation under the grounded ice sheet. All elevations are on the EIGEN-6C4 geoid (a.s.l). Dotted lines are grounding line locations and solid lines are subglacial drainage. Backgrounds are Landsat imagery listed in Table S2.

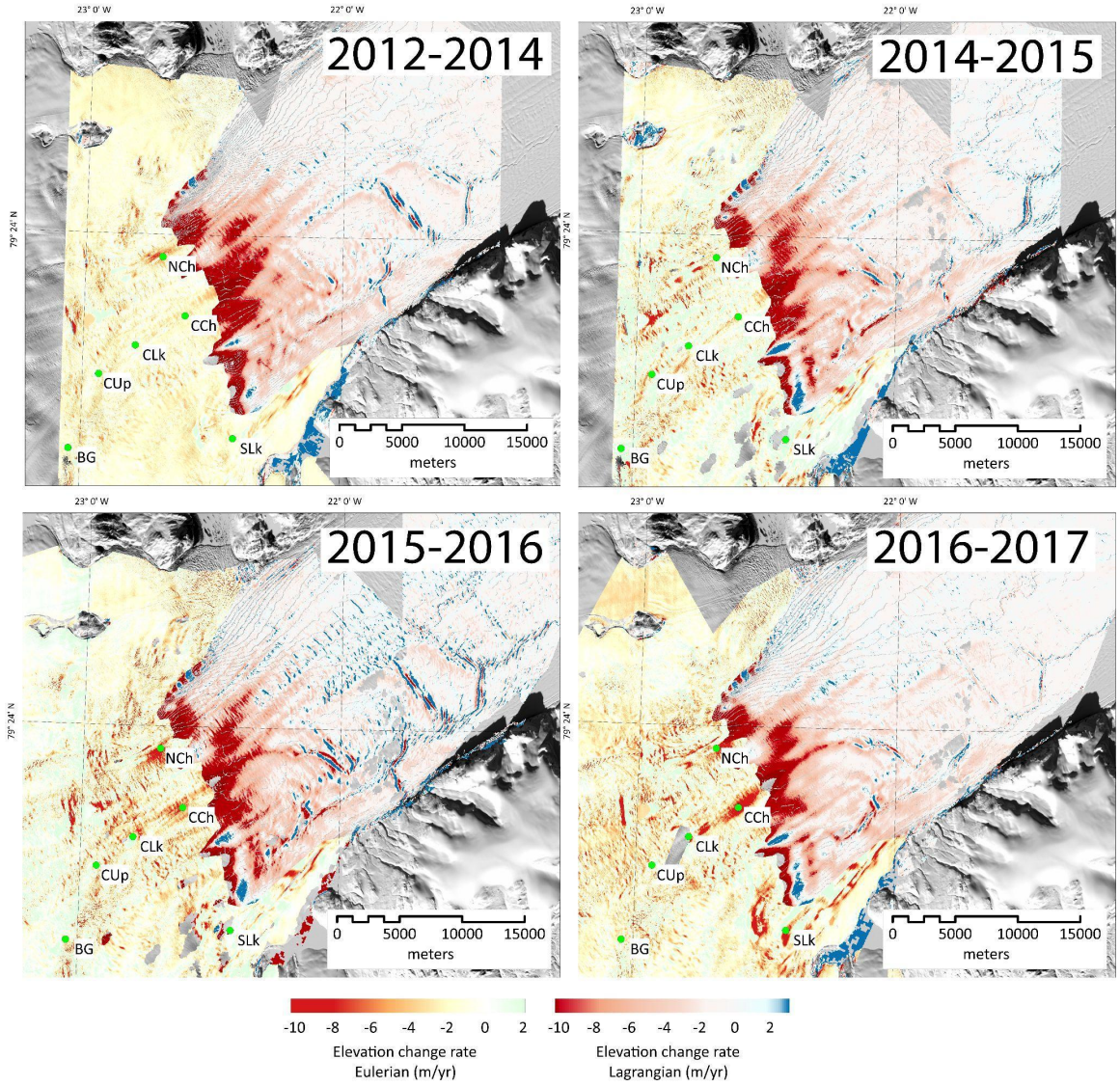

Figure S6. Annual thickness change rates between Spring of 2012-2014, 2014-2015, 2015-2016 and 2016-2017. Eulerian thinning (fixed reference frame) is shown over grounded ice and Lagrangian thinning (moving reference frame) on floating ice.

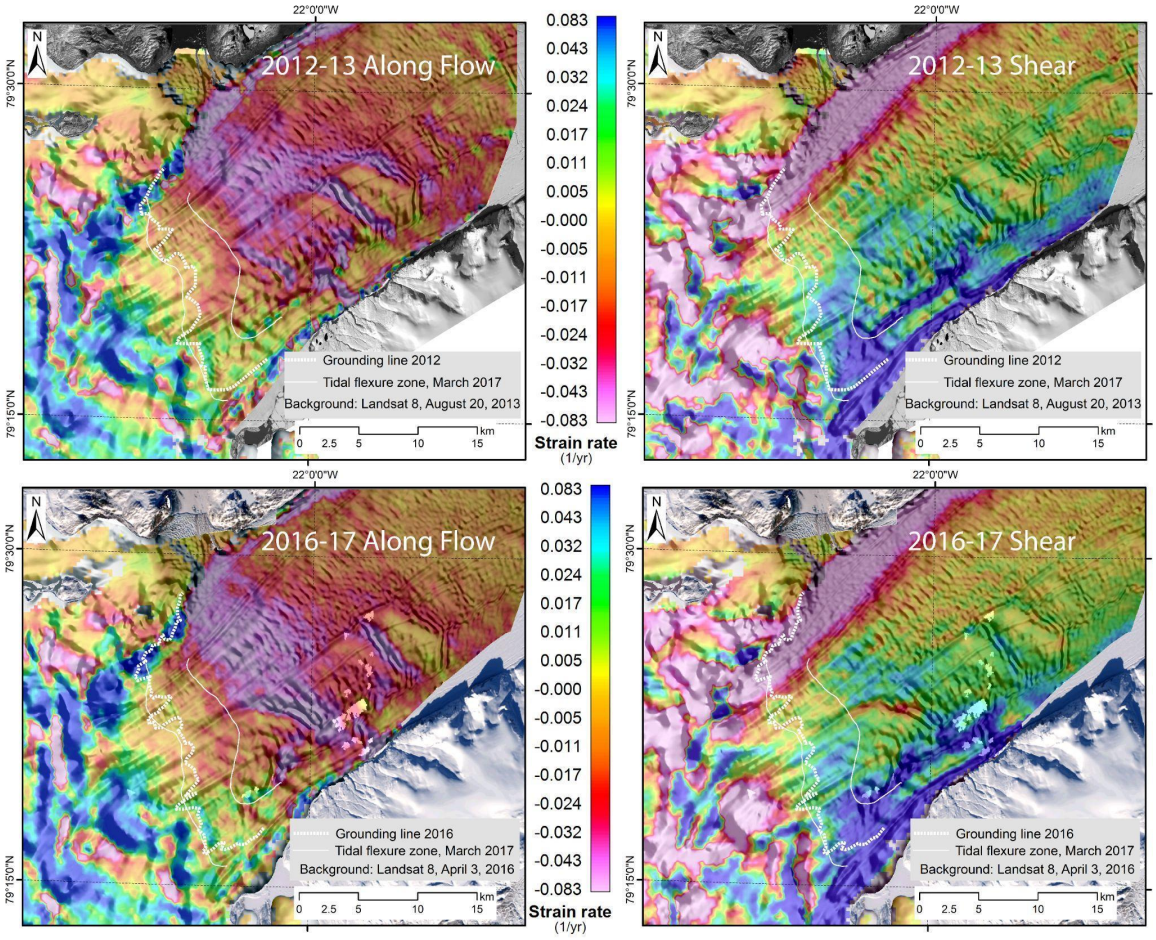

Figure S7. Along- and across- flow strain rate components from annual average velocity overlain in 2012-13 and 2016-17 on shaded relief DEMs. Background is Landsat 8 imagery (Table S2). 2016-17 strain rates are also shown in Figure 4 and included here for easy comparison.

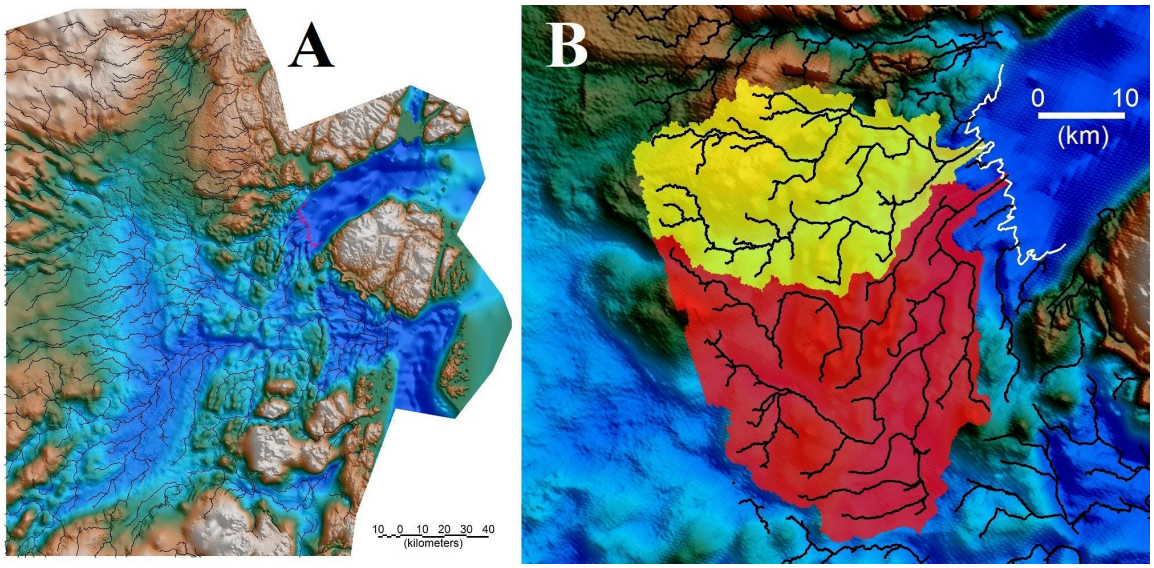

Figure S8. Subglacial routing over bed topography in 2017 (A), with extent of subglacial drainage basin boundaries on grounded ice (B).

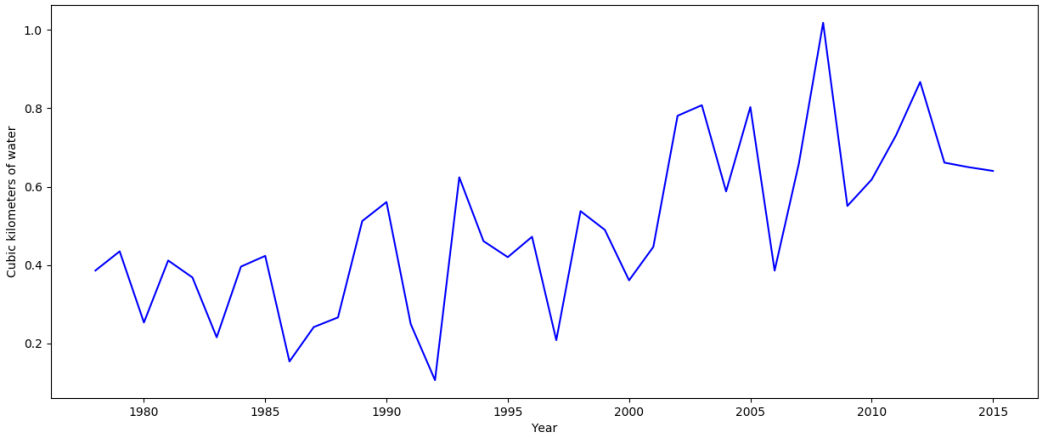

Figure S9. Cumulative runoff within the N79 drainage basin (Fig. S8 red and yellow regions combined) for the years 1978-2016.

Table S1 List of DEMs used for each reconstruction

Table S1A. 2012 Reconstruction, nominal date: 6/12/2012

Mosaic Order	ArcticDEM Filename
1	WV02_20120427_1030010017442400_1030010017B34300_seg1_2m_v3.0
2	WV01_20120430_10200100198A9500_1020010018D64700_seg1_2m_v3.0
3	WV01_20120621_102001001B348A00_102001001AA65A00_seg1_2m_v3.0
4	WV01_20120515_102001001BD59B00_102001001B4BAF00_seg1_2m_v3.0
5	WV01_20120531_102001001B433100_102001001B2D1C00_seg1_2m_v3.0
6	WV01_20120531_102001001B772400_102001001B530900_seg1_2m_v3.0
7	WV01_20120622_102001001C358B00_102001001B849800_seg1_2m_v3.0
8	WV01_20120514_102001001A7F8100_102001001BE40F00_seg1_2m_v3.0
9	WV01_20120805_102001001C9B5A00_102001001A32DB00_seg1_2m_v3.0
10	WV02_20120801_103001001AD82300_103001001A1E1200_seg4_2m_v3.0
11	WV02_20120417_1030010012816700_1030010013109E00_seg1_2m_v3.0

Table SB. 2014 Reconstruction, nominal date: 4/5/2014

Mosaic Order	ArcticDEM Filename
1	WV01_20140405_102001002DC0DF00_102001002CAEC500_seg1_2m_v3.0
2	WV01_20140323_102001002D294100_102001002FA8DD00_seg1_2m_v3.0
3	WV02_20140408_1030010030AA1D00_103001002F63F100_seg1_2m_v3.0
4	WV02_20140323_103001002E792700_103001002F822700_seg1_2m_v3.0
5	WV01_20140427_102001002ED1EA00_102001002D2F1100_seg2_2m_v3.0

Table S1C. 2015 Reconstruction, nominal date: 4/14/2015

Mosaic Order	ArcticDEM Filename
1	WV01_20150406_102001003DD47D00_102001003B1A2900_seg1_2m_v3.0
2	WV02_20150415_1030010041B3DF00_10300100405F0900_seg1_2m_v3.0
3	WV03_20150406_10400100092E6500_104001000A6E9400_seg1_2m_v3.0
4	WV03_20150420_104001000A388800_104001000A155100_seg1_2m_v3.0
5	WV02_20150419_1030010041026D00_1030010041B9F400_seg1_2m_v3.0
6	WV03_20150419_104001000A800900_104001000A064400_seg1_2m_v3.0
7	WV01_20150417_102001003C929A00_102001003B825400_seg1_2m_v3.0

Table S1D. 2016 Reconstruction, nominal date: 3/26/2016

Mosaic Order	ArcticDEM Filename
1	WV03_20160320_104001001ABCA500_104001001A749100_seg1_2m_v3.0
2	WV01_20160404_102001004C2E5000_102001004992DA00_seg1_2m_v3.0
3	W1W1_20160331_102001004992DA00_102001004D8C6D00_seg1_2m_v3.0
4	WV01_20160331_1020010050710900_102001004D8C6D00_seg1_2m_v3.0
5	WV02_20160317_1030010054AE2600_103001005327A800_seg1_2m_v3.0
6	WV02_20160320_103001005341D700_1030010052688600_seg1_2m_v3.0
7	WV03_20160321_104001001994D300_1040010019BC8700_seg1_2m_v3.0
8	WV02_20160323_103001005314A300_1030010053A89300_seg1_2m_v3.0

Table S1E. 2017 Reconstruction, nominal date: 3/27/2017

Mosaic Order	ArcticDEM Filename
1	WV01_20170411_1020010061672400_102001006117A500_seg1_2m_v3.0
2	WV01_20170403_102001005D62FB00_102001005D08D300_seg1_2m_v3.0
3	WV03_20170320_104001002AC32A00_104001002B8CB000_seg1_2m_v3.0
4	WV02_20170317_10300100660BAA00_10300100650DD100_seg1_2m_v3.0
5	WV03_20170327_104001002A23AD00_10400100296CB400_seg1_2m_v3.0
6	WV03_20170326_104001002B0F7700_104001002B29B500_seg1_2m_v3.0
7	WV03_20170326_104001002A6FB700_104001002A69F800_seg1_2m_v3.0
8	WV01_20170330_102001005E45E900_102001005A66CE00_seg1_2m_v3.0

Table S1F. 2020 Reconstruction, nominal date: 6/5/2020

Mosaic Order	ArcticDEM Filename
1	SETSM_s2s041_WV02_20200927_10300100AD1B3600_10300100B07B9D00_2m_lsf_seg1
2	SETSM_s2s041_WV02_20200820_10300100AB446100_10300100AC7C1F00_2m_lsf_seg1
3	SETSM_s2s041_WV03_20200328_104001005838AF00_104001005947AB00_2m_lsf_seg1
4	SETSM_s2s041_WV02_20200324_10300100A5145500_10300100A2381A00_2m_lsf_seg1
5	SETSM_s2s041_WV02_20200406_10300100A3776100_10300100A5C08300_2m_lsf_seg1
6	SETSM_s2s041_WV02_20200717_10300100A9337000_10300100AC499B00_2m_lsf_seg1
7	SETSM_s2s041_WV03_20200917_104001005E73FF00_104001005F2F4A00_2m_lsf_seg1
8	SETSM_s2s041_WV02_20200824_10300100AAD28400_10300100AC8E6B00_2m_lsf_seg8

Table S2 List of aerial and satellite images used as figure backgrounds

Date	Sensor	Full ID Name	Figures
Jul 3, 1978	Aerial camera	g150_1978_utm27_1&2 (orthophotographs)	1D, S1A, S1B
Aug 20, 2013	Landsat 8	LC08_L1TP_014002_20130820_20170502_01_T1_B8	S1, S5, S7
Aug 24, 2013	Landsat 8	LC08_L1TP_010002_20130824_20200912_02_T1_B8	S1
Aug 24, 2013	Landsat 8	LC08_L1TP_010002_20130824_20200913_02_T1_B8	S1
Sep 8, 2014	Landsat 8	LC08_L1TP_014002_20140908_20170419_01_T1_B8	S5
Sep 11, 2015	Landsat 8	LC08_L1TP_014002_20150911_20170404_01_T1_B8	S5
Apr 3, 2016	Landsat 8	LC08_L2SP_009003_20160403_20200907_02_T1_B4	4, S5, S7
Mar 30, 2017	Landsat 8	LC08_L2SP_008003_20170330_20200904_02_T1_B4	2, 3, S6
Aug 3, 2017	Landsat 8	LC08_L1TP_010003_20170803_20200903_02_T1_B4,3,2	1A, 1B, 1E, S5
Jun 29, 2020	Landsat 8	LC08_L1TP_013002_20200629_20200708_01_T1_B8	1F, S5

Supplemental Bibliography

Foerste, C., Bruinsma, S. L., Abrykosov, O., Lemoine, J.-M., Marty, J. C., Flechtner, F., Balmino, G., Barthelmes, F., Biancale, R. (2014). EIGEN-6C4 The latest combined global gravity field model including GOCE data up to degree and order 2190 of GFZ Potsdam and GRGS Toulouse. *GFZ Data Services.* https://doi.org/10.5880/icgem.2015.1

Padman, L., Siegfried, M. R., & Fricker, H. A. (2018). Ocean tide influences on the Antarctic and Greenland ice sheets. *Reviews of Geophysics*, 56, 142–184. doi: 10.1002/2016RG000546

Sutterley, T. C., Markus, T., Neumann, T. A., van den Broeke, M., van Wessem, J. M., Ligtenberg, S. R. M. (2019) Antarctic ice shelf thickness change from multimission lidar mapping. *The Cryosphere,* 13(7), 1801–1817. doi: 10.5194/tc-13-1801-2019